MDPI

Article

Sustainable Synthesis of Zirconium Dioxide (ZrO$_2$) Nanoparticles Utilizing *Asphodelus fistulosus* Extract for Congo Red Degradation

Rand A. N. Alkhalifa, Abuzar E. A. E. Albadri [ID], Reham Ali [ID], Abdullah H. Alluhayb *[ID], Alaa M. Younis and Sayed M. Saleh *[ID]

Department of Chemistry, College of Science, Qassim University, Buraidah 51452, Saudi Arabia;
431214181@qu.edu.sa (R.A.N.A.); aa.albadri@qu.edu.sa (A.E.A.E.A.); re.ali@qu.edu.sa (R.A.);
a.younis@qu.edu.sa (A.M.Y.)
* Correspondence: ah.alluhayb@qu.edu.sa (A.H.A.); e.saleh@qu.edu.sa (S.M.S.)

Abstract: This research presents a green approach to synthesizing zirconium oxide (ZrO$_2$) nanoparticles using an *Asphodelus fistulosus* plant extract as a reducing and stabilizing agent. The synthesized ZrO$_2$ nanoparticles were characterized using various advanced techniques. The XRD pattern provides different forms of ZrO$_2$, like tetragonal and cubic forms, and the results confirmed the successful formation of crystalline ZrO$_2$ nanoparticles with a definite morphology. The XPS data exhibit that the bioactive chemicals present in the extract, including polyphenols, flavonoids, and reducing sugars, perform the functions of reducing and capping agents. Additionally, CR dye molecules may create hydrogen bonds with these surface moieties, which are approved by FTIR. These interactions may assist in aligning dye molecules with catalytically active regions on ZrO$_2$ surfaces and may interact with photogenerated species. The catalytic activity of the synthesized ZrO$_2$ nanoparticles was evaluated for the degradation of Congo red dye under ultraviolet irradiation. The nanoparticles exhibited excellent photocatalytic activity, degrading a significant amount of the dye within a short period. Various parameters were investigated to optimize the photodegradation process, including irradiation time, catalyst dosage, pH, and initial dye concentration. The optimal conditions were determined to be a pH of 7, a catalyst loading of 20 mg/L, and an irradiation time of 75 min, resulting in a remarkable ≈92% degradation efficiency. This green synthesis method offers a sustainable and eco-friendly alternative to conventional chemical methods for producing ZrO$_2$ nanoparticles, which have potential applications in environmental remediation.

Keywords: green synthesis; ZrO$_2$; nanoparticles; degradation; *Asphodelus fistulosus*; photocatalysis

1. Introduction

The presence of dyes in water streams has ordinary impacts on organisms [1,2]. Many tons of dyes are produced worldwide; they are used by small- and large-scale enterprises such as tanneries and the food, cosmetic, textile, and pharmaceutical industries [3–5]. The textile industry is mostly responsible for dye emissions into the environment. The dyes' complex structures, which are made up of aromatic rings bound to various functional groups with an electron, can absorb light in the 380–700 nm range [6,7]. The presence of chromogens and chromophores gives them color. Several synthetic and natural dyes

are carcinogenic, although azo group proliferation has been linked to amine and benzidine emissions [8,9]. In addition, the dye molecules' inability to biodegrade prolongs their half-life in the environment, posing risks. It is, therefore, necessary to remove dye molecules from wastewater before releasing the stream into the environment, which could have both short- and long-term consequences [10,11]. Direct contact has been linked to serious consequences for aquatic life. On the other hand, observations of human reactions have ranged from skin irritations to diseases like cancer. Although several methods for treating dye-containing streams have been documented, research is still being conducted to determine the most effective method [12–15]. Based on recent studies, the textile industries use 10–12% of dyes annually, including Rhodamine B, Victoria blue, Rose Bengal, Indigo Red, Carmine, Red 120, Eriochrome, Methylene blue (MB), Crystal violet, and Methyl orange [16–19]. However, a significant amount (20%) of these dyes is lost during synthesis and processing, ending up in wastewater. The colored pigments in these dye-polluted effluents are highly toxic, non-biodegradable, and detrimental to living things [20,21]. Aquatic ecosystems are contaminated by dyes, visible in water even in very low quantities (less than 1 part per million). Therefore, it is critical to remove dyes from effluent [22,23].

Utilizing plant extracts for the purpose of producing zirconium dioxide (ZrO_2) nanoparticles is a strategy that is both environmentally benign and sustainable. This method substitutes potentially hazardous chemicals with natural substances that are present in plants. When it comes to the transformation of zirconium ions (Zr^{4+}) into nanoparticles, plant extracts, which are exceptionally abundant in bioactive compounds, serve as reducing and stabilizing agents. This technique not only lessens the amount of pollution released into the environment but also makes use of the distinctive qualities that plants possess to generate nanoparticles that can potentially be used in areas such as photocatalysis, medicine, and environmental remediation. One organic contaminant of concern to the environment is Congo red (CR) dye. It is a colorant in the rubber, textile, printing, and dyeing industries. The need to remove CR from industrial CR-laden (waste) water stems from the carcinogenicity, mutagenicity, and several related toxicities of CR for flora, wildlife, and humans [24–26]. Congo red (CR) is characterized by its permanent aromatic structure, which makes it non-biodegradable, and its detrimental effects on human health and aquatic species [27,28]. Numerous methods have been developed to remediate pollutants in wastewater. These processes include sedimentation, flocculation, coagulation, biological treatment, absorption/adsorption, physical and chemical treatment, and membrane processes [29–31].

Various kinds of nanoparticles, including first-, second- and third-generation nanomaterials, are employed in degrading dyes. Photodegradation is a process wherein photon absorption mainly breaks down a substance in (UV-visible) light. In the process, species develop and give rise to new ones. There are reports on the three types of photodegradation. Photolysis uses UV light energy to create reactive materials, such as ions or compounds with excited radicals. How the composite is arranged and the amount of energy transferred by radiation determine how the radiation affects the composite material. Through primary products created by photolysis of an aqueous solution, which produces electrons, (H·) radicals, and (OH·) radicals as intermediate species that break down the solute, this process is accelerated in aqueous media. When oxidants such as H_2O_2, O_3, or Fenton reagent are linked to photo-oxidation processes via UV light sources, the rate of deterioration is significantly higher than when UV is used alone. The primary oxidizing agents are the hydroxyl and per hydroxyl radicals that are momentarily produced in subsequent processes [32–34].

A photon-driven reaction aided by a catalyst is what photocatalysis is all about. The process starts when a photon is absorbed and has sufficient energy (equal to or more than the catalyst band gap energy). The catalyst's valence band and conduction band

support absorption owing to the separation of charge caused by the electron (e^-), creating a hole (h^+). The electron–hole pair can move to the catalyst's surface and enter the redox reaction by way of other materials that are present there. The electrical configuration of a chosen metal, which is classified by an empty conduction band and a filled valence band separated by a band gap or energy gap, may allow a variety of semiconductors, including TiO_2, Fe_2O_3, ZnO, ZnS, and CdS, to function as catalysts [35,36]. ZnO and TiO_2, two semiconductors widely employed as photocatalysts, are chosen because they are chemically and physiologically benign, readily obtained and used, and can catalyze reactions. These materials are less costly and safe for the environment and for people to use [37,38].

ZrO_2 nanoparticles were likely chosen for Congo red dye degradation due to their combination of desirable properties. Their high surface area maximizes contact with dye molecules, facilitating efficient adsorption and subsequent degradation. Furthermore, ZrO_2 exhibits excellent chemical stability, resisting corrosion and ensuring long-term reusability. Notably, ZrO_2 possesses inherent photocatalytic activity, particularly in its various crystalline phases, enabling the degradation of organic pollutants under light irradiation. Finally, ZrO_2 is considered a relatively environmentally friendly material compared to some other metal oxide catalysts, making it a promising candidate for sustainable dye degradation applications [39]. CR is widely utilized throughout several sectors, such as textile dyeing, paper printing, and food processing. This extensive utilization results in considerable environmental pollution. Congo red is recognized as hazardous to aquatic species and may adversely affect human health. The vivid red hue facilitates precise and efficient spectrophotometric observation of the degradation process. This streamlines experimental methodologies and data evaluation. Congo red has an intricate aromatic structure, rendering it a difficult contaminant to degrade [40].

The objective of this investigation was to synthesize a ZrO_2 nanocomposite using environmentally benign methodologies that are based on *Asphodelus fistulosus*. The purpose was to produce ZrO_2 NPs based on an *Asphodelus fistulosus* extract (*AF-ZrO_2 NPs*) and to assess their photocatalytic activity for the degradation of CR. The ZrO_2 NPs were characterized using a scanning electron microscope (SEM), energy-dispersive X-ray spectroscopy (EDX), Brunauer–Emmett–Teller surface area analysis (BET), X-ray diffraction (XRD), Fourier transform infrared spectroscopy (FTIR), and X-ray photoelectron spectroscopy (XPS). The photocatalytic activity was detected by examining the initial CR concentrations, pH parameters, and the dose of the nanoparticle that is required for catalysis. Additionally, mechanisms, kinetic experiments, and reusability were assessed.

2. Results

2.1. A Characterization of AF-ZrO_2 NPs

2.1.1. Morphology

The scanning electron microscope (SEM) is used to obtain high-magnification images of the surface morphology of materials [41,42]. It is possible to analyze the size, shape, and dispersion of the *AF-ZrO_2 NPs* seen in the image below by using scanning electron microscopy (SEM) photographs. As seen in the SEM images, the particles of *AF-ZrO_2* are quite uniform, with the majority falling within a certain size range. The diameter of *AF-ZrO_2 NPs* typically ranges from 20 to 40 nanometers, as shown in Figure 1A. When the size of the particles is a key aspect, such as in catalysis or when nanoparticles are employed as fillers in composites, this demonstrates that the particles were manufactured and controlled. This is particularly important in situations where the size of the particles is a role. The nanoparticles have a shape that is almost identical to one another. A modest degree of agglomeration of nanoparticles is seen, which is often anticipated in any nanoparticle

system due to the high surface energy of nanoparticles and, therefore, the inclination to lower their surface area by clustering.
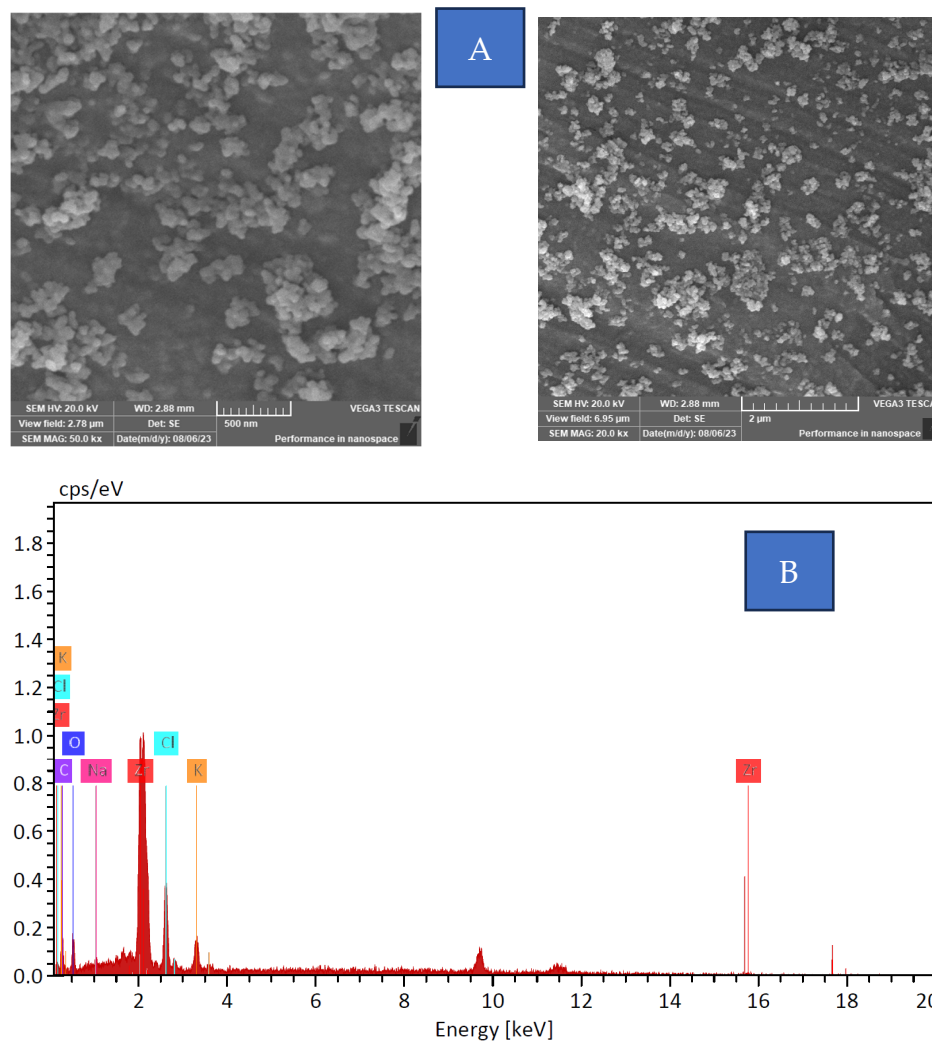

Figure 1. (**A**) SEM images of the *AF-ZrO$_2$ NPs* and (**B**) DX analysis of *AF-ZrO$_2$* sample.

2.1.2. EDX Analyses

Energy-dispersive X-ray spectroscopy (EDX), when coupled with scanning electron microscopy (SEM), provides insights into the elemental composition and chemical characteristics of the materials. EDX analysis indicates the elemental composition percentages in the *AF-ZrO$_2$* sample seen in the above picture. The EDX spectra and quantitative analysis indicate the existence of many elements in the *AF-ZrO$_2$* nanoparticles: zirconium (Zr), carbon (C), chlorine (Cl), oxygen (O), potassium (K), and sodium (Na). As anticipated, zirconium (Zr) has a mass percentage of 42.36%. The substantial quantity of zirconium indicates that the nanoparticles mainly comprise ZrO$_2$ (see Figure 1B). Oxygen constitutes 13.87% by mass, indicating its role as an oxide component of nanoparticles. Carbon was identified at 21.13% by mass. The elevated level may be ascribed to surface physisorption or the existence of carbonaceous species used during synthesis or sampling. Chlorine identified at 15.92% by mass may be attributable to residual chlorinated precursors or solvents used during synthesis. Potassium (K) and sodium (Na) are found in trace quantities, maybe as byproducts of the synthesis process or as impurities in the initial ingredients. The mass percentages of the components presented in the EDX analysis provide insights into the proportion of each constituent [43,44]. The numbers are normalized to 100% to illustrate the relative proportions of the items in the sample. The standard deviations, coefficients

of variation, and other related mistakes indicate the confidence level in the quantitative results. The relative error of zirconium is 4.24%, indicating a moderate level of accuracy in the measurement; all the data are provided in Table 1. In this context, components like sodium exhibit more significant relative errors, indicating less confidence in the precision of their measurement. The integration of SEM and EDX investigations yields a thorough comprehension of the *AF-ZrO₂* nanoparticles. The SEM and EDX characterization of *AF-ZrO₂* nanoparticles is essential for assessing particle size, morphology, and chemical composition. The well-defined spherical forms with polished surfaces and the elevated zirconium and oxygen content in all manufactured nanoparticles further corroborate the production of ZrO_2 nanoparticles. The existence of other components, including carbon, chlorine, potassium, and salt, emphasizes the need to prioritize purity and processing conditions. These nanoparticles possess many applications, and further characterization might enhance their characteristics and use. Additionally, an eco-friendly method of synthesis is utilized in the production of ZrO_2 nanoparticles by utilizing the extract of *Asphodelus fistulosus*. This method uses the natural chemicals present in the plant extract to decrease and stabilize the nanoparticles. During the synthesis process, the bioactive chemicals present in the extract, including polyphenols, flavonoids, and reducing sugars, perform the functions of reducing and capping agents. This process is both environmentally benign and cost-effective, and it results in the production of ZrO_2 nanoparticles that possess distinctive characteristics such as their tiny size, various morphologies (such as nanospheres and nanorods), and impressive stability [45].

Table 1. EDX data of *AF-ZrO₂* sample.

Element	At. No.	Netto	Mass [%]	Mass Norm. [%]	Atom [%]	Abs. Error [%] (1 Sigma)	Rel. Error [%] (1 Sigma)
Zirconium	40	6645	22.70	42.36	12.47	0.96	4.24
Carbon	6	409	11.32	21.13	47.23	3.4	30
Chlorine	17	2251	8.53	15.92	12.06	0.39	4.54
Oxygen	8	492	7.43	13.87	23.27	2.11	28.38
Potassium	19	869	3.20	5.97	0.18	0.18	5.74
Sodium	11	116	0.40	0.75	0.08	0.08	20.15
	Sum		53.58	100.00		100.00	

2.1.3. XPS Analysis

The constituent profiles and their chemical structures were adequately understood through the XPS analysis of *AF-ZrO₂*. The metal analysis report delineates the chemical form of zirconium, while the survey chart contains the profile of zirconium and oxygen, as shown in Figure 2a. The incorporation of this analysis will facilitate the determination of the surface characterization and utilization of *AF-ZrO₂* in various applications. The XPS survey chart provides comprehensive information on all elements that are present on the surface of the sample substrate. Most frequently, it reveals peaks that are in accordance with the binding energies of core-level electrons, which are emitted from the atoms that comprise the sample under the influence of X-rays. Zr's existence is demonstrated by the binding energies of peaks associated with Zr(3d), Zr(3p), and other levels of Zr core shells [46]. These peaks indicate the material's composition, as it contains ZrO_2. The region of O 1s also exhibits peaks that resolve oxygen atoms, which is unavoidable given that ZrO_2 is composed of zirconium and oxygen. The N 1s peaks indicate that nitrogen is present, which may be derived from organic substances that are used to prepare *Asphodelus fistulosus*. The presence of contaminants in the environment or the sample preparation procedure can also result in the observation of a carbon peak, which is an individual member of the C 1s.

This is corroborated by the fact that the Zr 3d peak is a composite of multiple components with distinct chemical states. As seen in Figure 2b, it is expected that zirconium will exhibit an oxidation state of +4 in the ZrO_2 compound, which will be accompanied by binding energy peaks for $Zr(3d)_{5/2}$ and $Zr(3d)_{3/2}$ [47,48]. The precise binding energy values for the Zr(3d) peaks will be correlated with the oxidation state of zirconium. ZrO_2 typically exhibits the apex of Zr ($3d_{5/2}$) at 30.3–30.6 eV and for Zr ($3d_{3/2}$) at 182–185 eV.
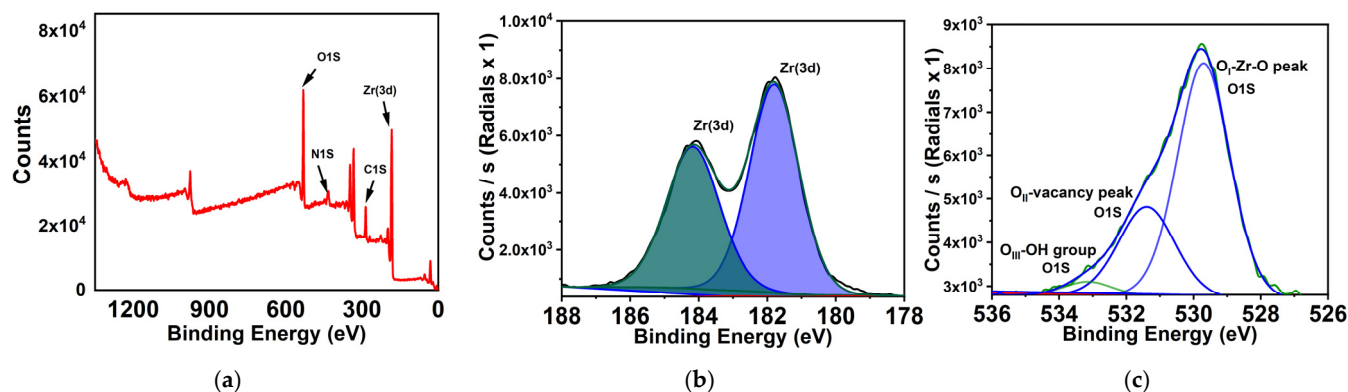

Figure 2. XPS analyses of *AF-ZrO₂*: (**a**) survey analyses; (**b**) Zr species analyses; and (**c**) oxygen spectrum.

The XPS study of ZrO_2 nanoparticles generated with the *Asphodelus fistulosus* plant extract indicates the existence of many oxygen species on the surface, including O-Zr-O bonds, oxygen vacancies, and hydroxyl groups as shown in Figure 2c. The surface characteristics, including oxygen vacancies and hydroxyl groups, are essential for augmenting the photocatalytic efficacy of the nanoparticles by serving as active sites for the adsorption and destruction of organic contaminants such as Congo red. The occurrence of these characteristics is likely ascribed to the impact of the plant extract during the synthesis process [49]. The BET surface area analysis results are included in the Supplementary Materials.

2.1.4. FTIR Analysis

FTIR spectra of *AF-ZrO₂* nanoparticles were recorded at 400–4000 cm^{-1} as provided in Figure 3. Most organic and inorganic moieties in the fingerprint area lie within this range; hence, it was chosen purposefully [50,51]. Thus, comparing spectra before and after CR dye degradation in nanoparticles reveals even slight changes in nanoparticle structure or surface properties. Both spectra have similar peak forms, which is clear. The core structure of *AF-ZrO₂* nanoparticles appears to resist photocatalysis, which is encouraging. Synthesized *AF-ZrO₂* nanoparticles have a prominent peak in the 3400–3500 cm^{-1} region, perhaps indicating an O-H stretching frequency in their FTIR spectra. This band responds to hydroxyl groups (OH^-) on ZrO_2 nanoparticles and water molecules' vibrational modes on the hydrophilic surface [52]. When exposed to radiation, ZrO_2 nanoparticles form electron–hole pairs. Surface hydroxyl groups can trap photogenerated holes (h^+) that migrate toward the surface. Trapping creates hydroxyl radicals (·OH). Therefore, it begins. Photocatalytic oxidation relies on ·OH radicals, which react with any organic contaminant, including CR dye [53]. Step-by-step oxidation of dye molecules produces simpler, less hazardous intermediates, including CO_2 and H_2O. The post-degradation FTIR spectrum reveals a slight O-H stretching band intensity drop. This spectrum shift shows that the dye degradation process involves surface hydroxyls and water. The following methods may explain this finding: the first is surface OH group consumption in ·OH radical production, which temporarily lowers their concentration.
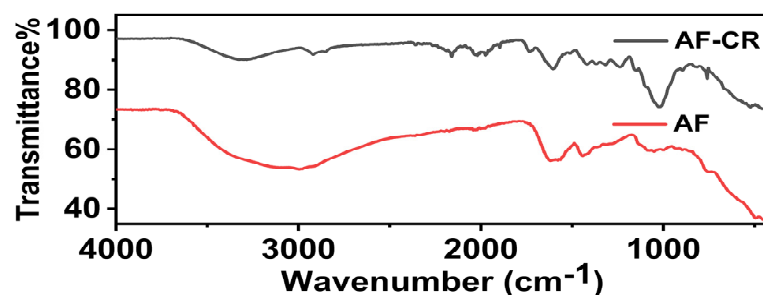
Figure 3. FTIR spectra of *AF-ZrO$_2$* and *AF-ZrO$_2$* after CR degradation.

Alternatively, CR dye molecules may create hydrogen bonds with these surface moieties. These interactions may assist in aligning dye molecules with catalytically active regions on ZrO$_2$ surfaces and may interact with photogenerated species. The bending vibrations of adsorbed water molecules cause a peak at 1630–1650 cm^{-1} on the wavenumber scale [54]. Remarkably, such a peak stays unchanged after dye breakdown, showing that the nanoparticle surface retains a lot of adsorbed water during photocatalysis. Since leftover water may perform several activities, it is not a passive spectator of dye degradation. At its simplest, the water layer may transport ·OH and superoxide radicals (O$_2$·−) from production sites to dye molecules. Hydrophilic water layers improved solvation and electrostatic interactions of ionic dyes like CR. Most intriguingly, these water molecules may participate in photocatalysis. Photogenerated holes can oxidatively damage them to produce additional ·OH radicals, boosting the system's oxidative capabilities. Peaks in the 400–800 cm^{-1} area represent the core of our *AF-ZrO$_2$* nanoparticles [55,56]. These bands represent stretching vibrations of Zr-O bonds in the ZrO$_2$ crystal lattice. The locations and their respective intensities provide valuable insights into the local coordination environment of Zr^{4+} ions and the nanoparticle structure. The absence of Zr-O peak shifts suggests that *AF-ZrO$_2$* nanoparticles are capable of this duty. They guarantee stiffness and the capacity to catalyze the reaction efficiently each time. This has considerable environmental and economic benefits: less catalyst replacement, waste creation, and treatment effects. The FTIR analysis becomes fascinating when we examine the absence of additional peaks of the same sort and a much higher level in the post-degradation spectrum. We can assume CR dye molecules establish stable complexes or covalent interactions with *AF-ZrO$_2$* nanoparticles.

2.1.5. XRD Analysis

The XRD pattern reveals the nanoparticles' crystalline structure and phase purity [57]. The figure shows intensity (in arbitrary units, a.u.) vs. 2θ (in degrees), with notable peaks with their Miller indices indicating the crystallographic planes responsible for the diffraction peaks as shown in Figure 4. Peaks are designated (100), (011), (100), (111), (002), (112), and (022). This XRD pattern is crucial as it provides valuable information about the ZrO$_2$ nanoparticles, including their size, shape, morphology, and optical characteristics [58]. Peak locations and intensities reveal the material's crystal structure, phase composition, and crystallinity [59]. Well-defined crystallographic planes in ZrO$_2$ nanoparticles indicate high structural order. By examining these peaks, we can identify different ZrO$_2$ phases, such as tetragonal and cubic [60]. This comprehensive characterization is essential for understanding the material's characteristics and prospective applications in catalysis, sensors, and biomedical devices [61]. XRD analysis plays a pivotal role in supporting ZrO$_2$ nanoparticle research and applications by demonstrating their structural integrity and enabling their utilization in numerous scientific and industrial applications [62].
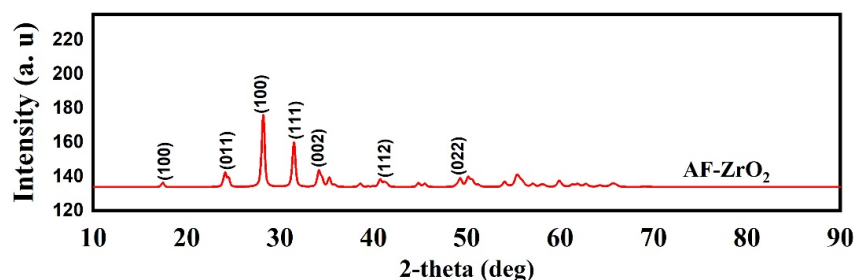
Figure 4. XRD patterns of *AF-ZrO₂ NPs*.

2.1.6. pH Effect

Congo red is a prevalent azo dye that is both persistent and poisonous, which is a cause for concern for the environment. To develop effective remediation solutions, it is necessary to comprehend the factors that contribute to the degradation of materials. Acidity, alkalinity, or pH values significantly influence degradation [63]. The initial pH of the solution is a critical variable in photocatalytic processes. It determines the ionization state of the catalyst surface and influences the electrical charge properties of the catalyst surface, both of which impact the degradation of the dye compounds. In general, the activity of different catalysts in photocatalytic reactions will fluctuate. These can all be attributed to the diverse pH levels of the contaminant and catalyst. However, it is difficult to determine how much pH influences the photo-degradation process because it serves multiple functions. The pH value influences the dissociation capacity of compounds, the charge distribution on the catalyst surface, and the oxidation potential of the catalyst's valence band [64].

The pH is a critical factor in dye adsorption onto a surface. The ionization levels of pollutants, the dissociation of functional groups on the active sites of the adsorbent, and the adsorbent's surface charge are all susceptible to pH values. This investigation aimed to examine the pH optimum on the capacity of ZrO_2 NPs to eliminate CR dye. The results in Figure 5 indicated that the adsorption efficacy experienced a significant increase using the slightly acidic medium but remained constant within the pH range of 2–4. This is because the adsorbent's surface has a positive charge. Further, a pH below 7 facilitates the binding of negatively charged dye molecules. At pH ≈ 6, the optimum removal efficiency is ≈85.4%. The efficacy of dye removal is diminished beyond pH 7 due to the repulsion between the dye molecules and the hydroxyl ions on the ZrO_2 NPs. The hydrolysis of the azo link under exceedingly alkaline (pH > 12) and severely acidic (pH < 2) conditions weakens the dye molecule, promoting cleavage and subsequent destruction. However, these extremes are exceedingly rare in most environmental settings. Photo-degradation: when exposed to UV light, water molecules' hydroxyl radicals (OH·) can degrade dye molecules, resulting in cleavage and mineralization. The production of OH· radicals is typically reduced by higher pH, which inhibits photo-degradation [65,66].
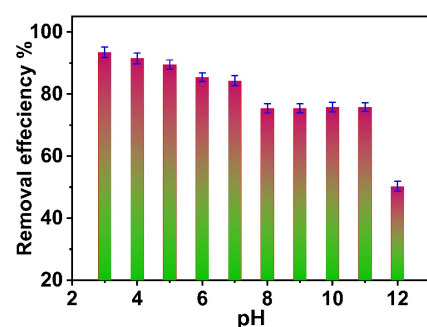

Figure 5. pH effect on the degradation of CR dye.

2.2. *Kinetic Study*

2.2.1. Effect of AF-ZrO$_2$ NPs Dosage

Congo red (CR) dye's photodegradation efficiency improves with increasing doses of the *AF-ZrO$_2$ NPs* photocatalyst within the range of 0 to 25 mg, peaking at 20 mg. As the dosage exceeds 20 mg, degradation efficiency declines due to increased turbidity, which reduces UV light penetration and limits the activation of additional nanoparticles. Thus, the ideal photocatalyst dose for optimal Congo red degradation is 20 mg, as shown in Figure 6. A UV-Vis graph to illustrate the calculation of % degradation and photodegradation efficiency is presented in the Supplementary Materials (See Figure S1).
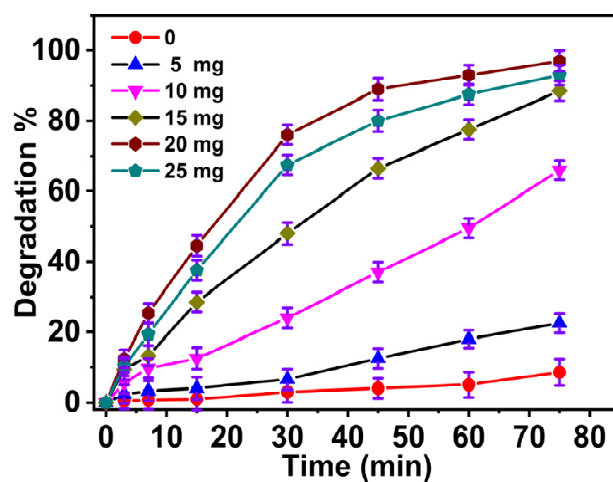

Figure 6. The degradation efficiency of CR versus time with different dosages of *AF-ZrO$_2$ NPs* in mg.

2.2.2. Effect of Initial Concentration of CR

Zirconium dioxide (ZrO$_2$) has a distinctive band structure, making it a significant material for photocatalytic applications. The bandgap of around 3.2 eV enables ZrO$_2$ to harness UV light for photocatalytic activities efficiently. The valence band of ZrO$_2$, consisting of oxygen 2p states, is positioned at a high energy level, whereas the conduction band, originating from zirconium 4p levels, is located at a significantly lower energy level [67]. This substantial energy disparity facilitates the dissociation of photoexcited electron–hole pairs, reducing recombination and improving photocatalytic performance. In photocatalytic reactions, photoexcited electrons in the conduction band and holes in the valence band engage in redox processes. Electrons may convert oxygen molecules to superoxide radicals, whereas holes can oxidize water molecules to hydroxyl radicals. These reactive species are particularly efficient in decomposing organic contaminants, disinfecting water, and executing different environmental remediation activities. The stability and non-toxicity of ZrO$_2$ enhance its appropriateness for sustainable and environmentally friendly photocatalytic processes.

Congo red degradation was studied at different initial concentrations between 10.0 and 60.0 ppm (see Figure 7). When using 20 mg of *AF-ZrO$_2$ NPs*, Congo red's degradation rate decreases. Higher concentrations cause more dye molecules to accumulate on the catalyst surface, reducing hydroxyl radical generation and blocking photon access to the photocatalyst surface. This results in a notable drop in photodegradation efficiency as CR concentration increases.
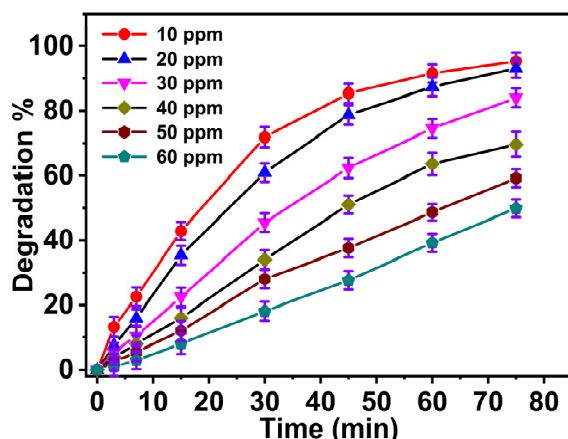
Figure 7. The effect of the initial concentration of CR ppm on the degradation efficiency in the presence of 20 mg of *AF-ZrO₂ NPs*.

2.2.3. First-Order Reaction

The slope of lines of ln(C$_0$/C) versus time [68]:

$$r = \frac{1}{k_1 k_2} \ln \frac{C_0}{C} + \frac{1}{k_2}(C_0 - C)$$

The degradation rate constant, K$_{app}$, decreases with increasing CR concentration, as shown in Figure 8, implying that high concentrations yield low degradation rates. This reduction in K$_{app}$ can relate to the coverage of the active sites on the surface of the photocatalyst and the growth of the absorption of the dye, which hinders the photons' access to the catalyst. For instance, at ten ppm, the rate constant k$_{app}$ is 41.5×10^{-3} min^{-1}; at 60 ppm and it reduces to 9.3×10^{-3} min^{-1} (Table 2). This marked drop supports the finding that higher initial concentrations of CR inhibit the photocatalytic degradation efficiency.
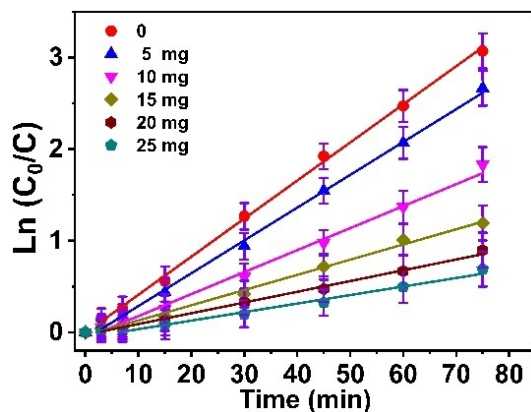

Figure 8. The plot of ln(C$_0$/C) versus time at different initial concentrations of CR.

Table 2. The apparent rate constants of CR degradation.

C$_0$ (ppm)	K$_{app}$. Min^{-1}
10	41.5×10^{-3}
20	35.8×10^{-3}
30	24.0×10^{-3}
40	16.6×10^{-3}
50	11.7×10^{-3}
60	9.30×10^{-3}

2.2.4. $t_{0.5}$ Versus C_0

The graph shows $t_{0.5}$ (half-life) versus initial CR concentrations (C_0), offering perceptions of the effect of concentration on the photodegradation rate. This linear plot has the equation $Y = 1.041x + 5.39$ with an R^2 value of 98.74, which shows a positive direct relationship between the two variables. The slope indicates that as the concentration of the initial CR rises, so does the time to half degradation. This trend suggests that increasing concentrations reduce the rate of photocatalyst degradation. Higher dye concentrations mean more molecules can absorb the UV light required to activate the photocatalyst. With the help of this figure, one can illustrate how the initial dye concentration can affect the degradation efficiency in the photocatalytic processes. The half-life of dye degradation at various initial concentrations was raised from the following Equation [69]:

$$t_{0.5} = \frac{C_0}{2k_2} + \frac{0.963}{k_1 k_2}$$

Figure 9 indicates a plot of $t_{0.5}$ versus C_0. The k_1 and k_2 values are 0.26 ppm and 0.248 ppm from the slope and intercept of the plot, respectively.
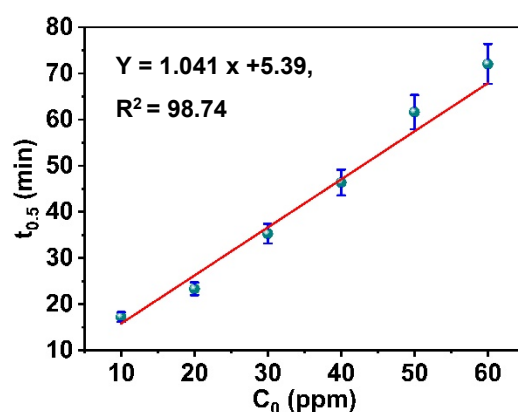

Figure 9. The plot of $t_{0.5}$ versus initial concentrations of CR.

2.3. Scavengers Effect (Mechanism)

The above outcome shows the impact of a range of scavengers on the breakdown of CR (reactive compound). The work shows how different scavengers affect the photocatalytic degradation mode. ASC (ascorbic acid) greatly retards degradation and must be presumed to be a potent inhibitor in the system, probably through interacting with holes or hydroxyl radicals [70]. However, degradation percentages for ISO (isopropanol) and systems without scavengers are high, implying their inefficiency in quenching active species that contribute to degradation. AgNO$_3$ (silver nitrate) and EDTA (ethylene diamine tetraacetic acid) also maintain high degradation rates, confirming that the presence of hydroxyl radicals, superoxide radicals, and holes play a critical role in the photocatalytic mechanism. Thus, the results suggest that while some scavengers (like ASC) inhibit photocatalysis by targeting key reactive species [71], others do not significantly interfere with the degradation process, as shown in Figure 10. The degradation of Congo red dye by ZrO$_2$ entails a photocatalytic mechanism in which ZrO$_2$ serves as a catalyst under ultraviolet illumination. UV light irradiation of ZrO$_2$ produces electron–hole pairs [72]. The photogenerated electrons in the conduction band and the holes in the valence band engage in redox processes. Electrons may decrease oxygen molecules to generate superoxide radicals, whereas holes can oxidize water molecules to obtain hydroxyl radicals [73]. These reactive species are proficient in decomposing the Congo red dye into smaller, less deleterious molecules, ultimately resulting in its destruction. Further, ZrO$_2$-AF predominantly absorbs ultraviolet light

owing to its extensive bandgap of around 3.2 eV. This indicates its capability to harness UV light for photocatalytic purposes efficiently. Nonetheless, ZrO_2 exhibits minimal visible light absorption, limiting its photocatalytic efficacy under such conditions. To improve its visible-light absorption, ZrO_2 is frequently amalgamated with other substances, such as graphitic carbon nitride (g-C_3N_4), to create composites capable of using a wider light spectrum. This combination can markedly enhance the photocatalytic efficacy of ZrO_2 under visible light [74].
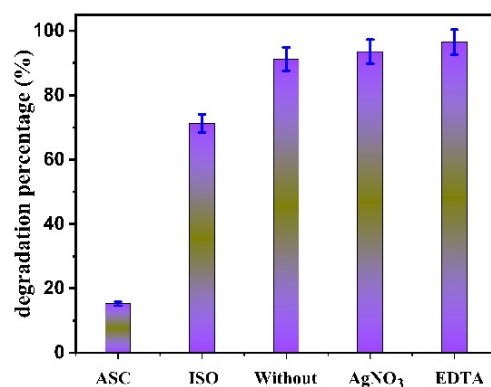

Figure 10. Scavengers effect on CR degradation.

2.4. The Effect of Photocatalysis Temperature

The results show how varying temperatures impact the photocatalytic degradation efficiency, showing consistent photodegradation across the tested temperature range. The degradation percentage remains high and nearly constant from 25 °C to 45 °C, suggesting that temperature variation within this range does not substantially influence the reaction kinetics or the activity of the photocatalyst, but it increases photodegradation slightly as provided in Figure 11. A slight dip at 50 indicates a threshold where higher temperatures start to destabilize or inhibit the photocatalytic process, potentially due to the desorption of reactants or the reduced formation of active radicals [75]. Thus, the results suggest that photocatalytic degradation is effective at room and slightly elevated temperatures but could decline at significantly higher temperatures.
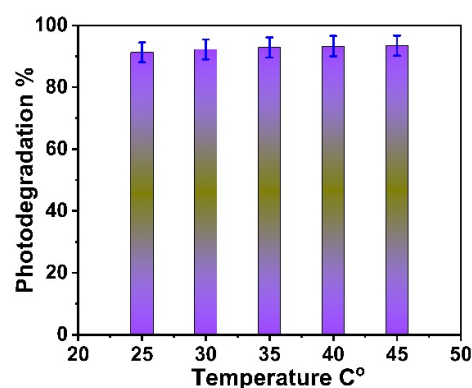

Figure 11. The effect of photocatalysis temperature.

2.5. Calcination of AF-ZrO₂ NPs Photocatalyst

The analysis of calcination temperature provides essential information on how to enhance the thermal characteristics of the *AF-ZrO₂ NPs* photocatalyst. The efficiency of photodegradation exhibits an evident temperature dependence within the range of 200–400 °C (see Figure 12). The catalyst performs best within the temperature range of

200–300 °C, wherein the photodegradation is notably high at 85–90%. This optimal temperature range probably defines the conditions under which the crystalline structure and surface of the ZrO_2 nanoparticles are most suitable for photocatalytic processes. Nonetheless, performance decreases rapidly at higher calcination temperatures of about 60% at 350 °C and 400 °C [76]. It is believed that these losses might be due to particle agglomeration, a reduction in surface area, and an undesired phase transformation, which are typical at high temperatures. The results indicate exact temperature regulation in the calcination process to enhance photocatalytic properties. Therefore, the temperature limit of 300 °C might damage the catalyst's efficiency.
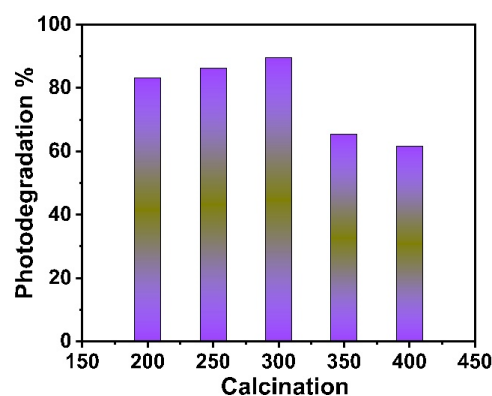

Figure 12. Calcination of *AF-ZrO₂ NPs* photocatalyst.

2.6. Recycling AF-ZrO₂ NP Photocatalyst for CR Degradation

This work offers valuable information regarding the recyclability and practical applicability of *AF-ZrO₂* NP photocatalysts in continuous water treatment processes. The first cycle achieves a high degree of photodegradation of around 95% and, as such, serves as a benchmark against which subsequent cycles can be measured. Five successive cycles demonstrate that the catalyst remains stable, incurring a loss of approximately 3–4% in efficiency through the fifth cycle while retaining roughly the same 80% degradation capability as provided in Figure 13. Such a slight decline in performance can be attributed to the structure's great strength and the absence of photo corrosion when used often. This might be due to the good adsorption of the active sites on the catalyst surface and good reactivity regeneration between cycles. The tiny loss in efficiency could be caused by a small aggregation of particles or just a small accumulation of particles on the surface, yet these impacts are minimal. Maintaining high catalytic performance after several cycles is relevant to potential usage in large-scale applications. It provides strong evidence that *AF-ZrO₂ NPs* may be a practical solution to the lengthy, expensive process of catalyst regeneration for large-scale purification and treatment of water.
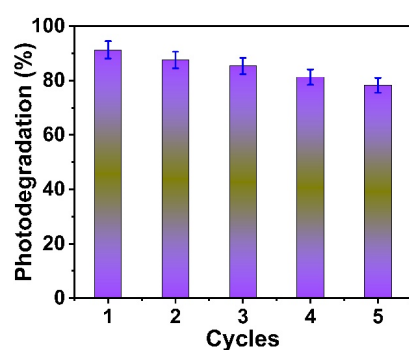

Figure 13. Photocatalytic reusability study of *AF-ZrO₂NP* photocatalyst for CR degradation.

2.7. Effect of Different Dyes

This makes a comparative study of the photocatalytic performance of the *AF-ZrO₂ NP* photocatalyst over a set of dye compounds truly insightful regarding its selectivity and efficiency profile. The highest degradation efficiency of about 80% is achieved with Indigo Carmine (IC), which yields much higher efficiency than all the other dyes studied in this work. Such a high performance with IC indicates a highly complementary relationship between the dye molecular structure and the active sites on the catalyst. Methyl Red (MR) and Methyl orange (MO) permit moderate removal efficiencies of 20–30%, whereas Congo red (CR) and Alizarin (Aliz) allow for a low percent of degradation of only 0–15% as shown in Figure 14. These significant differences in degradation rates from dye to dye may be due to differences in molecular size, chemical structure, charge distribution, and the kind and nature of interactions between the adsorbed dye molecules and the catalyst surface. A significant difference in the degradation efficiencies indicates that the photocatalytic process is selective and depends on the molecular size of the dye, the present functional groups, and their interaction with the catalyst surface. This understanding is fundamental in enhancing the catalyst profile in industries where certain dye compounds are most likely to be encountered.
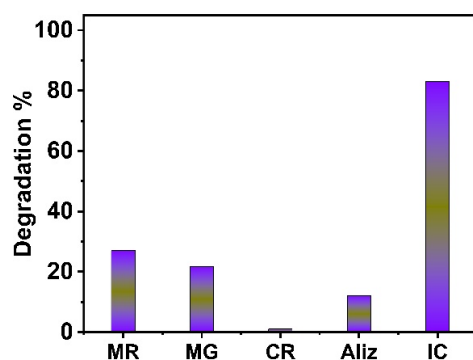

Figure 14. Different dyes photodegradation.

3. Materials and Methods

3.1. Materials

Figure S1 shows the plant *Asphodelus fistulosus* obtained from a reserve for seasonal wild plants in the Al-Rass area. The chemicals used in the synthesis, zirconyl chloride octahydrate ($ZrOCl_2.8H_2O$) and absolute ethanol (C_2H_5OH, $\geq$99%), were from Sigma Aldrich (Saint Louis, MO, USA). The utilized dyes, including Congo red (CR, $\geq$97%), Malachite green (MG, $\geq$90%), Crystal violet (CV, $\geq$90%), Methylene blue (MB, $\geq$82%), and Rhodamine 6G (RG $\geq$ 95%), were also brought from Sigma Aldrich. All chemicals were used without further purification.

3.2. Measurement Techniques:

The structure and crystalline characteristics of ZrO_2 nanoparticles were analyzed using an XD-2 (Shimadzu ED-720, Tokyo, Japan) powder X-ray diffractometer, operating at a voltage of 36 kV and a current of 20 mA, using CuK(α) radiation within the $5° < 2\theta < 75°$ range, with a wavelength of 1.54056 Å and a scanning rate of $1°$ min^{-1}. The morphology of the ZrO_2 NPs was examined using a QUANTA (Raleigh, NC, USA) FEC 250 scanning electron microscope. X-ray photoelectron spectroscopy (XPS) investigations were conducted using a K-ALPHA (Thermo Fisher Scientific, Waltham, MA, USA) equipped with monochromatic Al K-alpha X-ray radiation, ranging from 10 to 1350 eV, with a spot size of 400 μm, under a pressure of 10^{-9} mbar, employing a full-spectrum pass energy of 200 eV

and a narrow-spectrum pass energy of 50 eV. Also, an FT-IR spectrometer (Nicolet 5700 FT-IR spectrophotometer, Green Bay, WI, USA) was used to determine the vibration modes of ZrO_2 nanoparticles. Alizrarinsulphonate dye (Aliz), Indigo Carmine dye (IC), Malachite green dye (MG), and deionized water were used throughout the examination. For the Congo red dye, the molecular formula of CR is ($C_{32}H_{22}N_6Na_2O_6S_2$), the molecular mass is 696.66 g/mol, and the structure of CR is shown in Scheme 1.
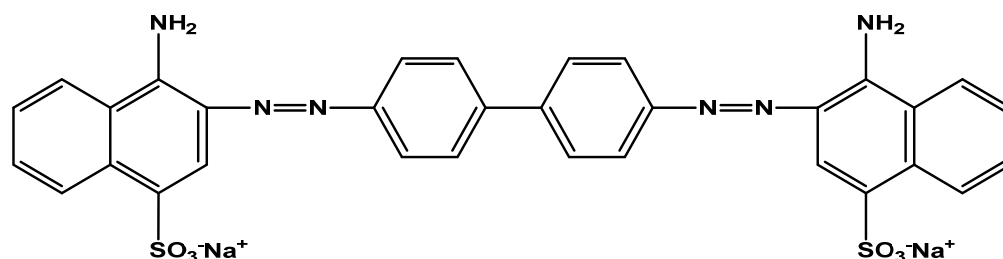
Scheme 1. The molecular structure of CR dye.

3.3. Aqueous Extract

The *Asphodelus fistulosus* was harvested. Then, the shooting system parts (stem, leaves, and flowers) were weighed individually and were carefully cut into pieces and washed with distilled water. The dried leaves were powdered into fine particles using a mixer grinder. For the preparation of aqueous leaf extract, 10 g of leaf *Asphodelus fistulosus* powder was dissolved in 100 mL of deionized water, followed by boiling for 4 h. Leaf extract was then left at room temperature until further use. Finally, it was filtered through Whatman 0.45 mm filter paper to obtain the pure leaf sample extract. The filtrate thus obtained was used as a plant extract.

3.4. Sustainable Production of AF-ZrO2 Nanoparticles

For the eco-friendly synthesis of ZrO_2 nanoparticles, 50 mL of a 0.1 M aqueous solution of zirconyl chloride octahydrate was placed in a 250 mL beaker. Subsequently, 10 mL of the plant extract was included and agitated at 90 °C for 4 h, after which the solution remained undisturbed. Following several days of incubation, nanoparticles were generated. The *AF-ZrO2 NPs* were obtained by evaporating the resultant solution in a vacuum air oven at 180 °C for 3 h. The product was then calcined at the optimum temperature.

3.5. Photodegradation Process

The photocatalytic degradation of CR was conducted under UV-A light irradiation utilizing a UV cabinet at a wavelength of 365 nm. A dye solution with a concentration of 10–60 ppm solutions were prepared in deionized water, and 0–25 mg of *AF-ZrO2* nanocomposites were included as a photocatalyst into 10 mL of the dye solution, which was subsequently agitated in a dark environment for specified durations to achieve equilibrium. Concentration and wavelength measurements were obtained by sampling the solution at certain time intervals using a spectrophotometer. Degradation was conducted both in the presence of and absence of light for each solution. The light was activated to commence the photocatalytic degradation reaction. Throughout irradiation, the solution was agitated continually to maintain homogeneity. The concentration of the dye solution was quantified using a UV spectrophotometer following the centrifugation of the deteriorated dye solution. The photocatalytic degradation studies of the dye were conducted until complete

degradation was achieved at designated time intervals. The degradation percentage was computed using the following equation [77]:

$$\text{Degradation \%} = \frac{C_0 - C}{C} \times 100$$

where C_0 represents the starting concentration of the CR dye, and C denotes the concentration of the dye post-UV-irradiation. A calibration curve was constructed by measuring the absorbance readings of samples with established concentrations.

4. Conclusions

Herein, we successfully synthesized ZrO_2 nanoparticles by employing a method that was ecologically friendly. We made use of the extract of the *Asphodelus fistulosus* plant with the purpose of decreasing and stabilizing the substance. To validate the crystalline structure and spherical shape of the nanoparticles that were created, characterization of these nanoparticles was carried out using various techniques. The degradation of Congo red dye was examined with ZrO_2 nanoparticles, and the findings demonstrated that the nanoparticles displayed catalytic activity when they were subjected to ultraviolet light. They achieved a high degradation efficiency of around 92% by changing elements such as the pH, catalyst dosage, and irradiation length to achieve the best possible outcomes. This research proves that green synthesis techniques could effectively manufacture photocatalysts that are both efficient and kind to the environment. The outcomes of this study give evidence that this possibility exists. In addition to contributing to the environmentally responsible rehabilitation of the environment, the production of ZrO_2 nanoparticles offers a potentially useful option for the breakdown of organic pollutants. The degradation of other persistent organic pollutants should be investigated using these nanoparticles in future research. Additionally, these nanoparticles' recyclability and long-term stability should be evaluated for practical applications, and the feasibility of scaling up the green synthesis process for potential industrial-scale wastewater treatment should be investigated.

Supplementary Materials: The following supporting information can be downloaded at: https://www.mdpi.com/article/10.3390/catal15020123/s1. Figure S1. Degradation of CR dye in the presence of *AF-ZrO2*. Figure S2. *Asphodelus fistulosus*.

Author Contributions: Conceptualization, S.M.S., R.A.N.A. and A.H.A.; methodology, R.A., A.E.A.E.A. and S.M.S.; formal analysis, S.M.S., R.A.N.A., A.E.A.E.A. and R.A.; investigation, S.M.S., R.A.N.A., A.H.A., A.M.Y. and A.E.A.E.A.; resources, S.M.S., A.H.A., A.E.A.E.A. and R.A.; data curation, S.M.S., A.H.A. and A.M.Y.; writing-original draft preparation, S.M.S. and R.A.N.A.; writing-review and editing, S.M.S.; supervision, S.M.S. and A.M.Y. All authors have read and agreed to the published version of the manuscript.

Data Availability Statement: All data will be made available upon reasonable request.

Conflicts of Interest: The authors declare no conflicts of interest.

References

1. Tkaczyk, A.; Mitrowska, K.; Posyniak, A. Synthetic organic dyes as contaminants of the aquatic environment and their implications for ecosystems: A review. *Sci. Total Environ.* **2020**, *717*, 137222. [CrossRef] [PubMed]
2. Sharma, S.; Kaur, A. Various methods for removal of dyes from industrial effluents—A review. *Indian J. Sci. Technol.* **2018**, *11*, 1–21. [CrossRef]

3. Navia-Mendoza, J.M.; Filho, O.A.E.; Zambrano-Intriago, L.A.; Maddela, N.R.; Duarte, M.M.M.B.; Quiroz-Fernández, L.S.; Baquerizo-Crespo, R.J.; Rodríguez-Díaz, J.M. Advances in the application of nanocatalysts in photocatalytic processes for the treatment of food dyes: A review. *Sustainability* **2021**, *13*, 11676. [CrossRef]

4. Adeel, S.; Abrar, S.; Kiran, S.; Farooq, T.; Gulzar, T.; Jamal, M. Sustainable application of natural dyes in cosmetic industry. In *Handbook of Renewable Materials for Coloration and Finishing*; Wiley: Hoboken, NJ, USA, 2018; pp. 189–211.

5. Alharbi, F.K.; Aissa MA, B.; Modwi, A.; Alharbi, A.A.; Alfadhl, F.; Saleh, S.M. Impact of Ag-NiO nanoparticles loaded on g-C$_3$N$_4$ nanosheets for cleaning contaminated water. *Inorg. Chem. Commun.* **2024**, *166*, 112608. [CrossRef]

6. Pizzicato, B.; Pacifico, S.; Cayuela, D.; Mijas, G.; Riba-Moliner, M. Advancements in sustainable natural dyes for textile applications: A review. *Molecules* **2023**, *28*, 5954. [CrossRef]

7. Saleh, S.M. Metal oxide nanomaterials as photo-catalyst for dye degradation. *Res. Dev. Mater. Sci* **2019**, *9*, 1–8. [CrossRef]

8. Saleh, S.M. ZnO nanospheres based simple hydrothermal route for photocatalytic degradation of azo dye. *Spectrochim. Acta Part A Mol. Biomol. Spectrosc.* **2019**, *211*, 141–147. [CrossRef]

9. Chung, K.T. Azo dyes and human health: A review. *J. Environ. Sci. Health Part C* **2016**, *34*, 233–261. [CrossRef]

10. Saleh, S.M.; Albadri, A.E.; Aissa, M.A.B.; Modwi, A. Fabrication of mesoporous V$_2$O$_5$@g-C$_3$N$_4$ nanocomposite as photocatalyst for dye degradation. *Crystals* **2022**, *12*, 1766. [CrossRef]

11. Saleh, S.M.; Ali, R.; Wolfbeis, O.S. New silica and polystyrene nanoparticles labeled with longwave absorbing and fluorescent chameleon dyes. *Microchim. Acta* **2011**, *174*, 429–434. [CrossRef]

12. Samsami, S.; Mohamadizaniani, M.; Sarrafzadeh, M.H.; Rene, E.R.; Firoozbahr, M. Recent advances in the treatment of dye-containing wastewater from textile industries: Overview and perspectives. *Process. Saf. Environ. Prot.* **2020**, *143*, 138–163. [CrossRef]

13. Sivagami, M.; Asharani, I.V. Phyto-mediated Ni/NiO NPs and their catalytic applications—A short review. *Inorg. Chem. Commun.* **2022**, *145*, 110054. [CrossRef]

14. Ravichandran, S.; Thangaraj, P.; Sengodan, P.; Radhakrishnan, J. Biomimetic facile synthesis of cerium oxide nanoparticles for enhanced degradation of textile wastewater and phytotoxicity evaluation. *Inorg. Chem. Commun.* **2022**, *146*, 110037. [CrossRef]

15. Younis, A.M.; Alminderej, F.M.; Alluhayb, A.H.; Saleh, S.M.; Aissa, M.A.B.; Modwi, A. Synergistic adsorption of methylene blue from aqueous medium using MgO-Y$_2$O$_3$@ gC$_3$N$_4$ (MYCN) nanocomposite: Performance evaluation and kinetic study. *Nano-Struct. Nano-Objects* **2024**, *39*, 101267. [CrossRef]

16. Katowah, D.F.; Saleh, S.M.; Mohammed, G.I.; Alkayal, N.S.; Ali, R.; Hussein, M.A. Ultra-efficient hybrid material-based cross-linked PANI@Cs-GO-OXS/CuO for the photocatalytic degradation of Rhodamine-B. *J. Phys. Chem. Solids* **2021**, *157*, 110208. [CrossRef]

17. Alharbi, F.K.; Albadri, A.E.; Modwi, A.; Saleh, S.M. Effectiveness of Ag@NiO@g-C$_3$N$_4$ photocatalysts: Green fabrication and superior photocatalysis capability. *Opt. Mater.* **2024**, *152*, 115410. [CrossRef]

18. Katowah, D.F.; Saleh, S.M.; Alqarni, S.A.; Ali, R.; Mohammed, G.I.; Hussein, M.A. Network structure-based decorated CPA@CuO hybrid nanocomposite for methyl orange environmental remediation. *Sci. Rep.* **2021**, *11*, 5056.

19. Ben Aissa, M.A.; Modwi, A.; Albadri, A.E.; Saleh, S.M. Dependency of crystal violet dye removal behaviors onto mesoporous V$_2$O$_5$-g-C$_3$N$_4$ constructed by simplistic ultrasonic method. *Inorganics* **2023**, *11*, 146. [CrossRef]

20. Weldegebrieal, G.K. Synthesis method, antibacterial and photocatalytic activity of ZnO nanoparticles for azo dyes in wastewater treatment: A review. *Inorg. Chem. Commun.* **2020**, *120*, 108140. [CrossRef]

21. Mehra, S.; Singh, M.; Chadha, P. Adverse impact of textile dyes on the aquatic environment as well as on human beings. *Toxicol. Int.* **2021**, *28*, 165. [CrossRef]

22. Tahir, U.; Yasmin, A.; Khan, U.H. Phytoremediation: Potential flora for synthetic dyestuff metabolism. *J. King Saud Univ. Sci.* **2016**, *28*, 119–130. [CrossRef]

23. Khandare, R.V.; Govindwar, S.P. Phytoremediation of textile dyes and effluents: Current scenario and future prospects. *Biotechnol. Adv.* **2015**, *33*, 1697–1714. [CrossRef] [PubMed]

24. Siddiqui, S.I.; Allehyani, E.S.; Al-Harbi, S.A.; Hasan, Z.; Abomuti, M.A.; Rajor, H.K.; Oh, S. Investigation of Congo red toxicity towards different living organisms: A review. *Processes* **2023**, *11*, 807. [CrossRef]

25. Mota, T.R.; Kato, C.G.; Peralta, R.A.; Bracht, A.; de Morais, G.R.; Baesso, M.L.; de Souza, C.G.M.; Peralta, R.M. Decolourization of Congo red by Ganoderma lucidum laccase: Evaluation of degradation products and toxicity. *Water Air Soil Pollut.* **2015**, *226*, 351. [CrossRef]

26. Oladoye, P.O.; Bamigboye, M.O.; Ogunbiyi, O.D.; Akano, M.T. Toxicity and decontamination strategies of Congo red dye. *Groundw. Sustain. Dev.* **2022**, *19*, 100844. [CrossRef]

27. Sayed, M.A.; Mohamed, A.; Ahmed, S.A.; El-Sherbeeny, A.M.; Al Zoubi, W.; Abukhadra, M.R. Enhanced photocatalytic degradation of Congo red dye into safe end-products over ZnO@ polyaniline/coal composite as low cost catalyst under visible light: Pathways and ecotoxicity. *J. Photochem. Photobiol. A Chem.* **2024**, *456*, 115843. [CrossRef]

28. Kaur, J.; Mudgal, G.; Negi, A.; Tamang, J.; Singh, S.; Singh, G.B.; Bose, K.J.C.; Debnath, S.; Wadaan, M.A.; Farooq Khan, M.; et al. Reactive black-5, Congo red and methyl orange: Chemical degradation of azo-dyes by agrobacterium. *Water* **2023**, *15*, 1664. [CrossRef]

29. Alminderej, F.M.; Albadri, A.E.; El-Ghoul, Y.; El-Sayed, W.A.; Younis, A.M.; Saleh, S.M. Sustainable and Green Synthesis of Carbon Nanofibers from Date Palm Residues and Their Adsorption Efficiency for Eosin Dye. *Sustainability* **2023**, *15*, 10451. [CrossRef]

30. Saleh, S.M.; Soliman, A.M.; Sharaf, M.A.; Kale, V.; Gadgil, B. Influence of solvent in the synthesis of nano-structured ZnO by hydrothermal method and their application in solar-still. *J. Environ. Chem. Eng.* **2017**, *5*, 1219–1226. [CrossRef]

31. Ismail, M.; Albadri, A.; Ben Aissa, M.A.; Modwi, A.; Saleh, S.M. High poisonous Cd ions removal by $Ru\text{-}ZnO\text{-}g\text{-}C_3N_4$ nanocomposite: Description and adsorption mechanism. *Inorganics* **2023**, *11*, 176. [CrossRef]

32. Zada, A.; Khan, M.; Khan, M.A.; Khan, Q.; Habibi-Yangjeh, A.; Dang, A.; Maqbool, M. Review on the hazardous applications and photodegradation mechanisms of chlorophenols over different photocatalysts. *Environ. Res.* **2021**, *195*, 110742. [CrossRef] [PubMed]

33. Salem, I. Recent studies on the catalytic activity of titanium, zirconium, and hafnium oxides. *Catal. Rev.* **2003**, *45*, 205–296. [CrossRef]

34. Chetoui, A.; Belkhettab, I.; Elfiad, A.; Messai, Y.; Ziouche, A.; Tablaoui, M. An in-depth photoluminescence investigation of charge carrier transport in ZrO_2/V_2O_5 type I junction: Probing the production of hydroxyl radicals. *Appl. Surf. Sci.* **2024**, *646*, 158947. [CrossRef]

35. Viswanathan, B. Photocatalytic degradation of dyes: An overview. *Curr. Catal.* **2018**, *7*, 99–121. [CrossRef]

36. Nemiwal, M.; Zhang, T.C.; Kumar, D. Recent progress in $g\text{-}C_3N_4$, TiO_2 and ZnO based photocatalysts for dye degradation: Strategies to improve photocatalytic activity. *Sci. Total Environ.* **2021**, *767*, 144896. [CrossRef]

37. Gnanaprakasam, A.; Sivakumar, V.M.; Sivayogavalli, P.L.; Thirumarimurugan, M. Characterization of TiO_2 and ZnO nanoparticles and their applications in photocatalytic degradation of azodyes. *Ecotoxicol. Environ. Saf.* **2015**, *121*, 121–125. [CrossRef]

38. Amini, M.; Ashrafi, M. Photocatalytic degradation of some organic dyes under solar light irradiation using TiO_2 and ZnO nanoparticles. *Nanochem. Res.* **2016**, *1*, 79–86.

39. Kumari, N.; Sareen, S.; Verma, M.; Sharma, S.; Sharma, A.; Sohal, H.S.; Mehta, S.K.; Park, J.; Mutreja, V. Zirconia-based nanomaterials: Recent developments in synthesis and applications. *Nanoscale Adv.* **2022**, *4*, 4210–4236. [CrossRef]

40. Magalhães, F.F.; Pereira, A.F.; Cristóvão, R.O.; Barros, R.A.; Faria, J.L.; Silva, C.G.; Freire, M.G.; Tavares, A.P. Recent Developments and Challenges in the Application of Fungal Laccase for the Biodegradation of Textile Dye Pollutants. *Mini-Rev. Org. Chem.* **2024**, *21*, 609–632. [CrossRef]

41. Fathima, J.B.; Pugazhendhi, A.; Venis, R. Synthesis and characterization of ZrO_2 nanoparticles-antimicrobial activity and their prospective role in dental care. *Microb. Pathog.* **2017**, *110*, 245–251. [CrossRef]

42. Malhat, F.; Abdallah, O.I.; Hussien, M.; Youssef, A.M.; Alminderej, F.M.; Saleh, S.M. Enhanced Adsorption of Azoxystrobin from Water by As-Prepared Silica Nanoparticles. *Coatings* **2023**, *13*, 1286. [CrossRef]

43. Gonbadi, M.; Sabbaghi, S.; Rasouli, J.; Rasouli, K.; Saboori, R.; Narimani, M. Green synthesis of ZnO nanoparticles for spent caustic recovery: Adsorbent characterization and process optimization using I-optimal method. *Inorg. Chem. Commun.* **2023**, *158*, 111460. [CrossRef]

44. Ammar, H.R.; Saleh, S.M.; Sivasankaran, S.; Albadri, A.E.; Al-Mufadi, F.A. Investigation of Element Migration from Aluminum Cooking Pots Using ICP-MS. *Appl. Sci.* **2023**, *13*, 13119. [CrossRef]

45. Tran, T.V.; Nguyen, D.T.C.; Kumar, P.S.; Din, A.T.M.; Jalil, A.A.; Vo, D.V.N. Green synthesis of ZrO_2 nanoparticles and nanocomposites for biomedical and environmental applications: A review. *Environ. Chem. Lett.* **2022**, *20*, 1309–1331. [CrossRef]

46. Dubey, S.; Kumar, V.; Dubey, K.; Sahu, C.; Modi, A.; Gautam, U.K.; Sharma, R.K.; Haque, F.Z.; Pagare, G.; Gaur, N.K. Tailoring the structural and electro-optical properties of avisible-light emitting $BaZrO_3$ photocatalyst: Integrating DFT and comprehensive experimental analysis. *Nanoscale* **2024**, *16*, 18086–18107. [CrossRef]

47. Idczak, K.; Mazur, P.; Zuber, S.; Markowski, L.; Skiścim, M.; Bilińska, S. Growth of thin zirconium and zirconium oxides films on the n-GaN (0 0 0 1) surface studied by XPS and LEED. *Appl. Surf. Sci.* **2014**, *304*, 29–34. [CrossRef]

48. Barreca, D.; Battiston, G.A.; Gerbasi, R.; Tondello, E.; Zanella, P. Zirconium dioxide thin films characterized by XPS. *Surf. Sci. Spectra* **2000**, *7*, 303–309. [CrossRef]

49. Chelliah, P.; Wabaidur, S.M.; Sharma, H.P.; Majdi, H.S.; Smait, D.A.; Najm, M.A.; Iqbal, A.; Lai, W.C. Photocatalytic organic contaminant degradation of green synthesized ZrO_2 NPs and their antibacterial activities. *Separations* **2023**, *10*, 156. [CrossRef]

50. Guerrero-Pérez, M.O.; Patience, G.S. Experimental methods in chemical engineering: Fourier transform infrared spectroscopy—FTIR. *Can. J. Chem. Eng.* **2020**, *98*, 25–33. [CrossRef]

51. Nandiyanto, A.B.D.; Oktiani, R.; Ragadhita, R. How to read and interpret FTIR spectroscope of organic material. *Indones. J. Sci. Technol.* **2019**, *4*, 97–118. [CrossRef]

52. Ghosh, A.; Raha, S.; Dey, S.; Chatterjee, K.; Chowdhury, A.R.; Barui, A. Chemometric analysis of integrated FTIR and Raman spectra obtained by non-invasive exfoliative cytology for the screening of oral cancer. *Analyst* **2019**, *144*, 1309–1325. [CrossRef] [PubMed]

53. Abd El-Aal, M.; Mogharbel, R.T.; Ibrahim, A.; Almutlaq, N.; Zoromba, M.S.; Al-Hossainy, A.F.; Ibrahim, S.M. Synthesis, characterization, and photosensitizer applications for dye-based on ZrO_2-acriflavine nanocomposite thin film [ZrO_2+ ACF] C. *J. Mol. Struct.* **2022**, *1250*, 131827. [CrossRef]

54. Yusuf, M.O. Bond characterization in cementitious material binders using Fourier-transform infrared spectroscopy. *Appl. Sci.* **2023**, *13*, 3353. [CrossRef]

55. Annu, A.; Sivasankari, C.; Krupasankar, U. Synthesis and characerization of ZrO_2 nanoparticle by leaf extract bioreduction process for its biological studies. *Mater. Today Proc.* **2020**, *33*, 5317–5323. [CrossRef]

56. Chau, T.P.; Kandasamy, S.; Chinnathambi, A.; Alahmadi, T.A.; Brindhadevi, K. Synthesis of zirconia nanoparticles using Laurus nobilis for use as an antimicrobial agent. *Appl. Nanosci.* **2023**, *13*, 1337–1344. [CrossRef]

57. Cullity, B.D.; Stock, S.R. *Elements of X-Ray Diffraction*; Prentice Hall: Upper Saddle River, NJ, USA, 2001; p. 388.

58. Suryanarayana, C.; Norton, M.G.; Suryanarayana, C.; Norton, M.G. *X-Rays and Diffraction*; Springer: New York, NY, USA, 1998; pp. 3–19.

59. Holder, C.F.; Schaak, R.E. Tutorial on powder X-ray diffraction for characterizing nanoscale materials. *ACS Nano* **2019**, *13*, 7359–7365. [CrossRef]

60. Sai, G.; Anna, V.R.; Swapna, K.; Prasad, M.S.; Ch, R.P.; Krishna, B.C.; Mandhala, V.N.; Madhav, B.T.P.; Praveenkumar, S.; Saleh, S.M.; et al. Evaluating the effects of sugarcane juice-mediated ZnO nanofluids on solar light activation for enhancing double-slope solar still performance. *Appl. Mater. Today* **2025**, *42*, 102542. [CrossRef]

61. Tuller, H. Ionic conduction and applications. In *Springer Handbook of Electronic and Photonic Materials*; Springer: Berlin/Heidelberg, Germany, 2017; Volume 1.

62. Alsehli, B.R.; Alminderej, F.M.; Hassan, M.H.; Al-Hakkani, M.F.; Saleh, S.M.; Mohamed, D.S. Biosynthesis, characterizations, and comparison of TiO_2/CeO_2/their nanocomposites as bio-adsorbents of linezolid and their microbiological activities. *J. Mol. Struct.* **2025**, *1328*, 141388. [CrossRef]

63. Zhu, S.; Wang, D. Photocatalysis: Basic principles, diverse forms of implementations and emerging scientific opportunities. *Adv. Energy Mater.* **2017**, *7*, 1700841. [CrossRef]

64. Zhu, J.; Holmen, A.; Chen, D. Carbon nanomaterials in catalysis: Proton affinity, chemical and electronic properties, and their catalytic consequences. *ChemCatChem* **2013**, *5*, 378–401. [CrossRef]

65. Shanker, U.; Rani, M.; Jassal, V. Degradation of hazardous organic dyes in water by nanomaterials. *Environ. Chem. Lett.* **2017**, *15*, 623–642. [CrossRef]

66. Shinde, S.S.; Bhosale, C.H.; Rajpure, K.Y. Kinetic analysis of heterogeneous photocatalysis: Role of hydroxyl radicals. *Catal. Rev.* **2013**, *55*, 79–133. [CrossRef]

67. Shaposhnikov, A.V.; Gritsenko, D.V.; Petrenko, I.P.; Pchelyakov, O.P.; Gritsenko, V.A.; Erenburg, S.B.; Bausk, N.V.; Badalyan, A.M.; Shubin, Y.V.; Smirnova, T.P.; et al. The atomic and electron structure of ZrO_2. *J. Exp. Theor. Phys.* **2006**, *102*, 799–809. [CrossRef]

68. Vinayagam, R.; Singhania, B.; Murugesan, G.; Kumar, P.S.; Bhole, R.; Narasimhan, M.K.; Varadavenkatesan, T.; Selvaraj, R. Photocatalytic degradation of methylene blue dye using newly synthesized zirconia nanoparticles. *Environ. Res.* **2022**, *214*, 113785. [CrossRef]

69. Vishnuganth, M.A.; Remya, N.; Kumar, M.; Selvaraju, N. Photocatalytic degradation of carbofuran by TiO_2-coated activated carbon: Model for kinetic, electrical energy per order and economic analysis. *J. Environ. Manag.* **2016**, *181*, 201–207. [CrossRef]

70. Mirsalari, S.A.; Nezamzadeh-Ejhieh, A. Focus on the photocatalytic pathway of the CdS-AgBr nano-catalyst by using the scavenging agents. *Sep. Purif. Technol.* **2020**, *250*, 117235. [CrossRef]

71. Zor, S.; Budak, B. Photocatalytic degradation of congo red by using PANI and PANI/ZrO_2: Under UV-A light irradiation and dark environment. *Desalination Water Treat.* **2020**, *201*, 420–430. [CrossRef]

72. Tanzifi, M. A Review on Application of Noble Metal-Free Materials/ZrO_2 Nano-photocatalysts for Removal of Organic Pollutants and Heavy Metals. *J. Water Environ. Nanotechnol.* **2024**, *9*, 263–286.

73. Fanourakis, S.K.; Barroga, S.Q.; Mathew, R.A.; Peña-Bahamonde, J.; Louie, S.M.; Perez, J.V.D.; Rodrigues, D.F. Use of polyaniline coating on magnetic MoO_3 and its effects on material stability and visible-light photocatalysis of tetracycline. *J. Environ. Chem. Eng.* **2022**, *10*, 107635. [CrossRef]

74. Wang, R.; Hu, Y.; Du, J.; Xu, L.; Fu, Y. Boosting the visible-light activity of ZrO_2/gC_3N_4 by controlling the crystal structure of ZrO_2. *J. Mater. Res.* **2021**, *36*, 3086–3095. [CrossRef]

75. Ilyas, M.; Ullah, S.; Khan, S.; Ahmad, A.; Rahman, F.; Khan, S. Zirconium Nanoparticles It's Biological Synthesis and Biomedical Application: A Review. *Plant* **2022**, *10*, 59–68.

76. Bagheri, S.; TermehYousefi, A.; Do, T.O. Photocatalytic pathway toward degradation of environmental pharmaceutical pollutants: Structure, kinetics and mechanism approach. *Catal. Sci. Technol.* **2017**, *7*, 4548–4569. [CrossRef]

77. Riede, A.; Helmstedt, M.; Riede, V.; Zemek, J.; Stejskal, J. In situ polymerized polyaniline films. 2. Dispersion polymerization of aniline in the presence of colloidal silica. *Langmuir* **2000**, *16*, 6240–6244. [CrossRef]